



Article

# Fatigue Behavior of As-Built L-PBF A357.0 Parts

Elena Bassoli <sup>1,\*</sup> , Lucia Denti <sup>1</sup>, Andrea Comin <sup>2</sup>, Antonella Sola <sup>1</sup>  and Emanuele Tognoli <sup>1</sup>

<sup>1</sup> Department of Engineering “Enzo Ferrari”, University of Modena and Reggio Emilia, via Pietro Vivarelli 10, 41125 Modena, Italy; lucia.denti@unimore.it (L.D.); antonella.sola@unimore.it (A.S.); emanuele.tognoli@unimore.it (E.T.)

<sup>2</sup> Maserati S.p.A., via Emilia Ovest 911, 41123 Modena, Italy; andrea.comin@maserati.com

\* Correspondence: elena.bassoli@unimore.it; Tel.: +39-059-205-6252

Received: 3 August 2018; Accepted: 8 August 2018; Published: 11 August 2018



**Abstract:** Laser-based powder bed fusion (L-PBF) is nowadays the preeminent additive manufacturing (AM) technique to produce metal parts. Nonetheless, relatively few metal powders are currently available for industrial L-PBF, especially if aluminum-based feedstocks are involved. In order to fill the existing gap, A357.0 (also known as A357 or A13570) powders are here processed by L-PBF and, for the first time, the fatigue behavior is investigated in the as-built state to verify the net-shaping potentiality of AM. Both the low-cycle and high-cycle fatigue areas are analyzed to draw the complete Wohler diagram. The infinite lifetime limit is set to  $2 \times 10^6$  stress cycles and the staircase method is applied to calculate a mean fatigue strength of 60 MPa. This value is slightly lower but still comparable to the published data for AlSi10Mg parts manufactured by L-PBF, even if the A357.0 samples considered here have not received any post-processing treatment.

**Keywords:** additive manufacturing; laser-based powder bed fusion; aluminum; fatigue strength

## 1. Introduction

Additive manufacturing, also known as three-dimensional (3D) printing, includes a wide group of technologies that are able to produce a 3D part according to a Computer Aided Design (CAD) model by adding material one layer at the time until the desired shape is finished. With respect to conventional subtractive or formative methods such as extrusion, forging, machining, etc., AM allows for wider freedom in geometry, reduced design constraints, minor assembly and joining requirements, limited material waste, and a shorter time-to-market [1]. In addition, AM methods are often regarded as “near net shaping techniques”, even if the layered strategy at the core of AM inherently poses several issues about the surface finishing of printed parts, with a roughness commonly exceeding an Ra value of 10  $\mu\text{m}$  [2]. Moreover, even if optimized processing parameters may lead to almost fully dense parts, with densities exceeding 99.5%, some pores and microstructural defects are unavoidably present in AM parts, which may impact the mechanical behavior of finished constructs [3].

Originally developed for rapid prototyping, AM is now growing very rapidly in terms of production numbers and economic importance. According to recent estimations, the sale of AM products and services is expected to grow from US \$5.2 billion in 2015 to over US \$26.5 billion by 2021. If metal AM is considered, according to statistics, 1768 AM systems were sold in 2017, compared to 983 systems in 2016, thus scoring an impressive increase of nearly 80% [4].

Standard ISO/ASTM 52900-15 [5], which defines general principles and terminology for AM, groups AM techniques into seven categories, all of which are compatible with polymer feedstocks. However, only three of these processes, including powder bed fusion, direct energy deposition, and sheet lamination, also apply to metals. Among them, powder bed fusion (PBF) is emerging as the most promising one, on account of its flexibility in terms of part design and feedstock availability.

In PBF, thermal energy is used to selectively consolidate specific areas of the powder bed, which is a relatively thin layer of fresh powder (typically below 100  $\mu\text{m}$ ) evenly distributed on top of the previously consolidated powder layers. The heat input may be supplied by an electron beam, in electron beam melting (EBM), or by a laser beam, in laser-based powder bed fusion (L-PBF). In the latter case, consolidation may rely upon sintering (direct laser sintering, DLS, also known as selective laser sintering, SLS) or complete melting-solidification mechanisms (selective laser melting, SLM) [6]. As a rule, the energy conveyed to the powder bed is enough to affect not only the new powder layer, but also the material underneath, so as to provide interlayer bonding [7].

At present, in spite of the increasingly widespread diffusion of AM in the industry, there is still a lack of understanding of the mechanical behavior of materials processed by L-PBF, especially aluminum and its alloys. In fact, L-PBF is mainly applied to steel, to titanium and its alloys, as well as to nickel, cobalt, molybdenum, and copper alloys [8]. However, the available formulations based on aluminum alloys are relatively few. Back in 2016, AlSi10Mg was the only aluminum feedstock on the market specifically intended for commercial L-PBF production [9]. Recently, AlSi12 was also investigated for aeronautic applications [10], but the palette of the available aluminum-based feedstocks for AM is currently very limited. Both economic and technical reasons have contributed to this delay. First of all, aluminum and its alloys, unlike titanium, are relatively easy and inexpensive to machine; therefore, processing them by AM may often prove to be economically counterproductive. From a technical standpoint, many aluminum alloys are hardly weldable. Besides this, common hardenable alloys contain elements, such as zinc, that are highly volatile, thus producing turbulent melt pools, splatter, and porosity during PBF. Additionally, aluminum has a very high reflectivity for the laser wavelengths that are usually employed in L-PBF [11]. Another hinderance is represented by the very low viscosity of molten aluminum that significantly reduces the size of the feasible melt pool. In fact, if the viscosity is low, the molten metal is likely to show better wettability, which is expected to enhance powder densification [12]. Nonetheless, if the viscosity is too low, the melt pool is not stable anymore and balling phenomena are likely to occur [13]. As a term of comparison, the viscosity of aluminum at its melting point (933.5 K) is as low as 1.34  $\text{mN}\cdot\text{s}/\text{m}^2$ , whereas the viscosity of titanium at its melting point (1958 K) is about three times as much, since it is 4.14  $\text{mN}\cdot\text{s}/\text{m}^2$  [14].

Even if the most common alloys for AM are the hardenable AlSi10Mg (for fatigue behavior, see References [15–25]) and the eutectic AlSi12 [10,26–28], new materials are emerging that require a systematic and coordinated effort to understand their optimal processing conditions and final properties [29,30].

A357.0 aluminum, also known as A357 or A13570 (with A357.0 being the Aluminum Association—American National Standards Institute (AA-ANSI) designation for this material [31]), is an aluminum alloy formulated for casting. In view of the approaching release of commercial A357.0 powders for AM, the present contribution is specifically addressed to determine the axial fatigue resistance of A357.0 parts produced by L-PBF and tested in their as-built state. A357.0 is a new entry on the market of commercial feedstocks for AM and hence very little is known so far about its properties. In fact, very few papers have been published to date on the production, microstructure, and mechanical properties of A357.0 parts manufactured by L-PBF [32–36]. It is worth noting that such articles are all very recent, since they have been published after 2016, which confirms the growing interest in this new aluminum alloy for L-PBF. The present contribution is therefore relevant with respect to the available literature on L-PBF processing of aluminum alloys because (i) it is specifically intended to investigate the fatigue behavior of A357.0 parts produced by L-PBF; (ii) it contributes to the qualification of new aluminum alloy-based AM parts that are currently the object of intensive research; and (iii) it sheds light on the real performance of AM parts in their as-built condition, thus verifying the asserted “near net shaping” nature of L-PBF.

In order to attain a deeper insight into the fatigue resistance of L-PBF A357.0 parts, in the present research tests were performed to define the complete Wohler diagram both in the low-cycle fatigue area, corresponding to high-stress failure, and in the high-cycle fatigue area, corresponding to low-stress

failure. This investigation paves the way for the statistical estimation of fatigue strength according to the staircase method.

## 2. Materials and Methods

### 2.1. AM Conditions

The specimens for the fatigue tests were manufactured on the X Line 2000R (Concept Laser GmbH, Lichtenfels, Germany) additive system according to the process parameters listed in Table 1.

The build platform was pre-heated in order to obtain an in situ aging effect, which made it possible to minimize the anisotropy of the finished part [15] and slow the cooling rate, thus reducing the residual stress state as compared to unheated parts [32]. For this reason, no stress-relieving treatment was performed on the built parts. In order to verify the “near net shaping” nature of L-PBF, all of the samples were tested in the as-built condition. The size and geometry for the fatigue test specimens conformed to the prescription for test pieces with tangentially blending fillets between the test section and the gripping ends as specified in standard UNI EN 3987:2010 [37]. Details are reported in Figure 1, where dimensions are expressed in millimeters. All samples were built parallel to the Z (build) direction, namely  $90^\circ$  with respect to the build platform, as shown in Figure 2. The Z building direction was chosen intentionally, since it is usually considered the most critical direction in PBF techniques [9,38].

**Table 1.** Process parameters applied on the X Line 2000R Concept Laser additive system to build the fatigue test specimens.

Process Parameter	Value
Laser power	950 W
Laser scan speed	2000 mm/s
Laser spot	400 $\mu\text{m}$
Hatch distance	0.2 mm
Layer thickness	50 $\mu\text{m}$
Inert gas	nitrogen
Platform pre-heating temperature	200 $^\circ\text{C}$
Scan strategy	skin-core

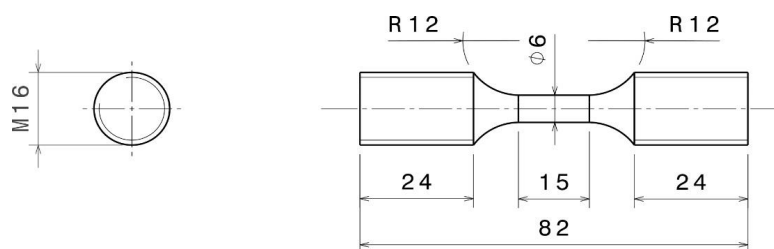


**Figure 1.** Geometry and size of the fatigue test specimens. Dimensions are expressed in millimeters.

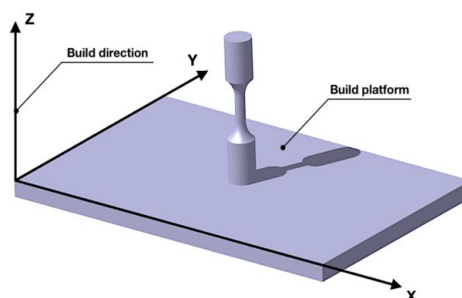


**Figure 2.** Built part orientation within the build chamber.

## 2.2. Axial Fatigue Tests

Axial fatigue tests were performed on an MTS 858 Mini Bionix II (MTS Systems Corp., Eden Prairie, MN, USA) instrument. Tests were conducted under ambient conditions with a relative humidity of about 40%. A cyclic frequency of 5 Hz and a stress ratio  $R = \sigma_{min}/\sigma_{max} = 0$  (origin) were used. The infinite lifetime limit was set to  $2 \times 10^6$  cycles for all tests. The applied testing procedures complied with two different standards to draw the Wohler diagram and to statistically estimate the fatigue strength.

### 2.2.1. Construction of the Wohler Diagram

Standard UNI EN 3987:2010 [37] was applied to draw the Wohler diagram. In brief, the standard provides the following guidelines to produce an S-N curve:

1. An initial test is performed at a peak stress level that is likely to induce a failure in  $1 \times 10^5$  cycles; according to the standard, if no other information is available but tensile test data exist, it is expected that an initial test at a stress of  $((UTS + 0.2\% PS)/2)$  will produce a failure, where *UTS* is the ultimate tensile stress and *0.2% PS* is the stress at which 0.2% plastic deformation occurs.
2. The peak stress level is reduced by 40 MPa for the next test; according to standard UNI EN 3987:2010, this stress reduction should produce a life in the order of  $1 \times 10^7$  stress-cycles unbroken. However, it is worth noting that the infinite lifetime limit in the present investigation was set to  $2 \times 10^6$  cycles, as previously stated.
3. If the test “2” fails before attaining the critical number of stress cycles, the peak stress level must be reduced by a further 20 MPa and the fatigue test must be repeated to provide an unbroken test result at the critical number of stress cycles.
4. The next test must be performed at a peak stress level up to 40 MPa higher than that used for the initial test “1”. This increment is expected to bring about a test endurance of around  $1 \times 10^4$  stress-cycles.
5. If the sample in test “4” is able to survive more than  $1 \times 10^4$  stress cycles, the peak stress must be increased by a further 20 MPa and the test must be repeated.
6. The procedure is repeated until any obvious gaps in the S-N curve are filled.

Since A357.0 parts processed by L-PBF are new to the scientific literature, previous information about the fatigue behavior was not available and therefore tensile data were determined according to standard UNI EN ISO 6892-1:2016 [39]. To this end, 17 samples were built parallel to the Z direction by applying the same processing parameters listed in Table 1 and following the size and geometry specifications included in the aforementioned standard UNI EN ISO 6892-1:2016 [39].

With the purpose of drawing the Wohler diagram, 13 samples were tested at different peak stress levels, as detailed in Table 2. In order to obtain average data, at least two samples were cycled at each stress level, except for low stress levels that were further investigated by means of the staircase method, as explained in Section 2.2.2. It is worth noting that the procedure described above matches the guidelines provided by standard UNI EN 3987:2010 [37] to draw the Wohler curve by using the minimum number of test pieces. The standard does not recommend any minimum number of samples to test for each stress level.

### 2.2.2. Statistical Estimation of Fatigue Strength

Standard ISO 12107:2012 (staircase method) [40] was applied to provide the mean value of the fatigue strength and an estimate of the standard deviation in spite of the widely scattered data that are often associated with the fatigue resistance of AM parts, especially in the high-cycle fatigue region [20]. Based on the standard, 15 test specimens were needed for exploratory research and they were tested according to the following general guidelines:

1. Rough estimates of the mean fatigue strength and related standard deviation should be known a priori. The first sample, randomly chosen, is tested at a peak stress level preferably close to the estimated mean fatigue strength. A stress step,  $d$ , is fixed preferably close to the standard deviation; if no other information is available,  $d$  can be assumed to be 5% of the estimated mean fatigue strength.
2. If the first specimen fails before reaching the given number of cycles ( $2 \times 10^6$  in the present test, as previously stated), the peak stress level for the next specimen is reduced by step  $d$ ; otherwise, if no failure occurs, the peak stress level for the next specimen is increased by the same step.
3. The procedure is repeated until all of the specimens have been tested.
4. The test data are rearranged in order to count the occurrence of “failure” and “non-failure” events of specimens tested at different stress levels; the statistical analysis must be applied to the group of events with the lower number of observations.
5. If  $S_0 \leq S_1 \leq \dots \leq S_l$  denote the stress levels arranged in ascending order, where  $l$  is the number of stress levels tested, and if  $f_i$  denotes the number of events associated with the  $S_i$  stress level and  $d$  denotes the stress step, the mean and the standard deviation of the fatigue strength at the given fatigue life are calculated from Equations (1) and (2), respectively:

$$\hat{\mu}_y = S_0 + d \left( \frac{A}{C} \pm \frac{1}{2} \right) \quad (1)$$

$$\hat{\sigma}_y = 1.62d(D + 0.029) \quad (2)$$

where:

$$A = \sum_{i=1}^l i f_i$$

$$B = \sum_{i=1}^l i^2 f_i$$

$$C = \sum_{i=1}^l f_i$$

$$D = \frac{BC - A^2}{C^2}$$

In Equation (1),  $(-1/2)$  is used when the analyzed event is failure;  $(+1/2)$  is used when the analyzed event is non-failure.

Equation (2) applies for  $D \geq 0.3$ . If this condition is not satisfied, the standard deviation can be estimated as [40,41]:

$$\hat{\sigma}_y = 0.53d \quad (3)$$

The equations are based on the assumption that the step size  $d$  lies in the interval  $0.5\hat{\sigma}_y$  to  $2.0\hat{\sigma}_y$ , where  $\hat{\sigma}_y$  is the standard deviation as calculated from Equation (2) or Equation (3).

Standard ISO 12107:2012 [40] also describes how to estimate the lower limit of the fatigue strength  $\hat{y}_{(P, 1-\alpha)}$  at a given probability  $P$  of failure, assuming a normal distribution, at the confidence level  $(1-\alpha)$  from the equation:

$$\hat{y}_{(P, 1-\alpha)} = \hat{\mu}_y - k_{(P, 1-\alpha, \nu)} \hat{\sigma}_y \quad (4)$$

where the coefficient  $k_{(P, 1-\alpha, \nu)}$  is the one-sided tolerance limit for a normal distribution and its value depends on the number of degrees of freedom,  $\nu$ , that was used in estimating the standard deviation (which is equal to the number of data items minus 1).

### 2.2.3. Analysis of Fracture Surfaces

The fracture surfaces of samples that failed under low-cycle fatigue conditions (peak stress level: 130 MPa) and under high-cycle fatigue conditions (peak stress level: 60 MPa) were observed with a scanning electron microscope, SEM (ESEM, Quanta FEI, Eindhoven, The Netherlands), operated in high vacuum mode.

### 3. Results

Representative stress-strain curves under tensile load are reported in Figure 3. The curves of 5 specimens are illustrated to show data repeatability. This figure also includes the tensile properties in terms of yield stress (0.2% PS), ultimate tensile stress (UTS), elasticity modulus ( $E$ ), and elongation to fracture ( $A_t$ ).

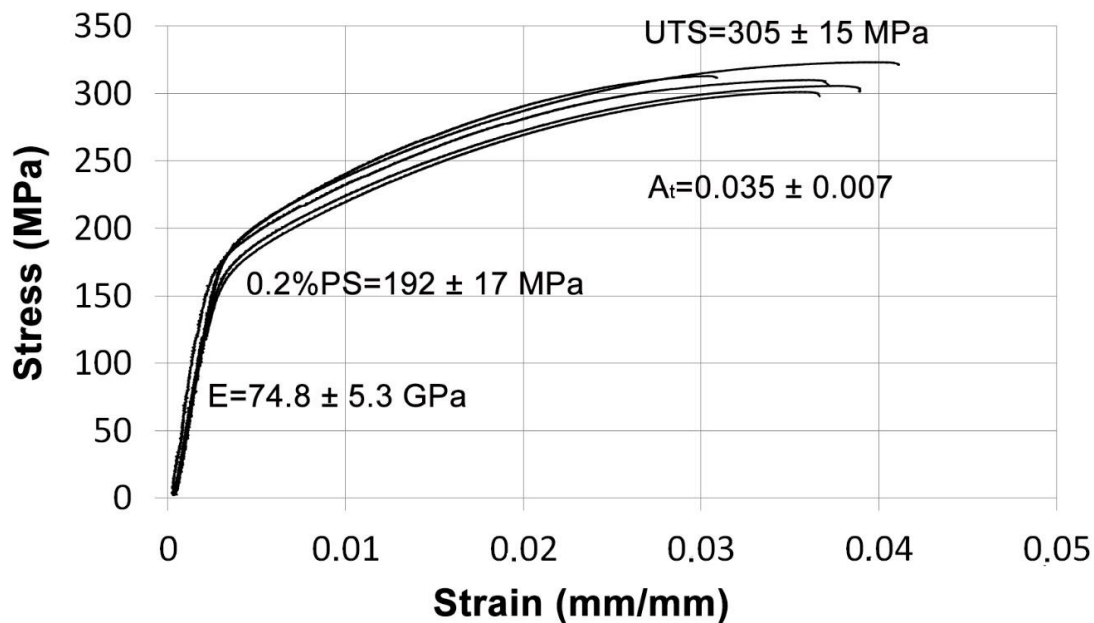


Figure 3. Static stress-strain curves and tensile properties.

The results of the axial fatigue tests conducted according to standard UNI EN 3987:2010 [37] are specified in Table 2. Based on the tensile tests, the value of  $UTS$  (ultimate tensile stress) and the value of 0.2% PS (the level of stress at which 0.2% plastic deformation occurs) for the specimens built parallel to the Z direction were found to be  $305 \pm 15$  MPa and  $192 \pm 17$  MPa, respectively (Figure 3). However, a preliminary axial fatigue test performed at a stress level of 240 MPa, which corresponded to  $(UTS + 0.2\% PS)/2$  as required by UNI EN 3987:2010 [37], led to a premature failure; this required lowering the stress level to below 200 MPa. Based on the experimental outcomes in Table 2, the fatigue strength at the given fatigue life of  $2 \times 10^6$  stress cycles could be preliminarily estimated at 50 MPa, which was thus the entry stress level for the staircase method.

The set of data obtained by means of the staircase method is given in Table 3. As shown in the last column in Table 3, the number of non-failures (i.e., 9) exceeded the number of failures (i.e., 6) and therefore the failure event was considered in the statistical analysis. Since at the lowest stress level (50 MPa) all samples survived, only two stress levels were considered in the statistical analysis, with  $S_0 = 60$  MPa and stress step  $d = 10$  MPa [42]. The results of the analysis are reported in Table 4.

With the coefficients in Table 4, the mean value of the fatigue strength at the given fatigue life of  $2 \times 10^6$  cycles could be calculated according to Equation (1) as  $\hat{\mu}_y = 60$  MPa. As to the standard deviation, Equation (3) was used, obtaining  $\hat{\sigma}_y = 5.3$  MPa. The basic condition  $0.5\hat{\sigma}_y (= 2.65) < d (= 10) < 2\hat{\sigma}_y (= 10.6)$  MPa was satisfied, thus confirming the validity of the staircase approach

applied here. Using the coefficients tabulated in standard ISO 12107:2012 [40] and the values for  $\hat{\mu}_y$  and  $\hat{\sigma}_y$  calculated above and introducing them in Equation (4), the lower limit at 10% probability of failure, at the confidence level of 95%, was calculated to be  $\hat{y}_{(10,95)} = 44$  MPa.

**Table 2.** Results of the axial fatigue strength tests conducted according to standard UNI EN 3987:2010 [37].

Maximum Stress (MPa)	Cycles to Failure
190	$4.0 \times 10^3$
190	$1.6 \times 10^4$
150	$2.5 \times 10^4$
150	$2.9 \times 10^4$
140	$5.8 \times 10^4$
140	$3.2 \times 10^4$
130	$5.1 \times 10^4$
130	$4.9 \times 10^4$
110	$9.5 \times 10^4$
110	$9.4 \times 10^4$
90	$1.7 \times 10^5$
70	$2.1 \times 10^5$
50	$>2 \times 10^6$

**Table 3.** Staircase test data obtained in accordance with standard ISO 12107:2012 [40]. “X” stands for a failure event; “O” stands for a non-failure event;  $S_i$  is the stress level applied.

$S_i$ (MPa)	Sequence Number of Specimens															X	O
	1	2	3	4	5	6	7	8	9	10	11	12	13	14	15		
70					X		X						X		O	3	1
60		X		O		O		X		X		O		O		3	4
50	O		O						O		O					0	4
																6	9

**Table 4.** Analysis of the data in Table 3.

Stress $S_i$	Level		Values	
	$i$	$f_i$	$i f_i$	$i^2 f_i$
$S_1 = 70$ (MPa)	1	3	3	3
$S_0 = 60$ (MPa)	0	3	0	0
Sum	—	$C = 6$	$A = 3$	$B = 3$

The complete Wohler diagram, which clearly shows a linear trend in log-log coordinates until the infinite life limit is reached, is drawn in Figure 4. The critical comparison of the fatigue results to the rare data published in the open literature becomes challenging, because diverse geometries and loading conditions are applied in different contributions. For example, it is known that the fatigue resistance at completely reversed stressing ( $R = -1$ ) is usually higher at rotating-bending than at tension-compression; for axial fatigue, the fatigue resistance at tension-compression, in its turn, is usually higher than that at tension-tension [15]. As a term of comparison, independent of the building orientation, the SLM AlSi10Mg specimens investigated by Mower and Long [9] achieved lower mechanical properties with respect to wrought Al6061, which was considered a benchmark. In more detail, the fatigue strengths of SLM AlSi10Mg parts were about 60% that of wrought Al6061. Indicatively, based on the Wohler diagram presented by Mower and Long [9], a cyclic stress amplitude of  $\sim 80$  MPa led to failure at  $7 \times 10^5$  cycles, whereas the  $1 \times 10^7$  cycle run-out was measured at  $\sim 55$  MPa for AlSi10Mg parts manufactured in the vertical direction and tested under the fully reversed rotating mode [9]. Quite interestingly, according to Mower and Long [9], the fatigue behavior was

not sensibly improved by surface finishing. The metallographic observation reported by Mower and Long [9] revealed the existence of numerous pores and microstructural faults distributed throughout the volume of the built parts. As a consequence, the surface finishing improved the surface roughness but revealed the sub-superficial defects that became new surface notches. Brandl et al. [15] instead proposed a “T6” thermal post-treatment, combined with a final surface finishing, as a possible way to increment the fatigue behavior of PBF aluminum alloy parts, which may pave the way for the future development of high-performance L-PBF A357.0 parts.

Siddique et al. investigated instead the fatigue behavior of AlSi12 parts processed by SLM, with and without base plate heating (200 °C) and stress relief (240 °C). All of the samples were surface-finished before testing. When the specimens were cycled under constant stress levels ( $R = -1$ ), the best results in terms of fatigue life were achieved by the parts without base plate heating and without stress relief that reached a fatigue life of about  $17.5 \times 10^4$  cycles under a cyclic load of 240 MPa. However, a very high fatigue scatter was observed as a consequence of the stochastic presence of large pores and defects. Heating the base plate slightly lowered the fatigue life, but it also substantially reduced the scatter. To the contrary, the effect of stress relief on specimens built on a heated base plate was negligible. The complete Wohler diagram showed that samples produced with base plate heating and then stress relief reached a fatigue strength of 80 MPa at  $10^7$  cycles, thus surpassing the greatest part of AlSi alloys processed by means of SLM, whose fatigue strength at  $10^7$  cycles is usually recorded in the range of 55 to 70 MPa [26].

Very recently, Yang et al. [36] proposed an accurate investigation of the relationship existing between process parameters and porosity development in A357.0 parts. In order to highlight the effects of porosity on the mechanical properties of finished parts, Yang et al. compared the fatigue behavior at  $R = 0.1$  with a frequency of 100 Hz of three different kinds of samples, namely (i) as-built samples (no sub-surface porosity removal; no surface finishing); (ii) surface machined samples (no sub-surface porosity removal); and (iii) machined samples without sub-surface porosity. After printing, each sample was thermally treated through stress relief, solution heat treatment, and artificial aging. Quite interestingly, the authors observed that the machined samples without sub-surface porosity reached a fatigue limit ( $10^7$  cycles) at a stress level of 175 MPa. However, the fatigue life was significantly reduced in the presence of sub-surface pores, independent of the surface roughness. In fact, the fatigue behavior was similar both for machined samples with sub-surface pores and for samples in their as-built state. The authors therefore concluded that, for this aluminum alloy, the fatigue behavior is influenced by the presence of sub-surface defects rather than by the surface roughness.

The results published by Yang et al. [36] appear to be complementary, rather than superimposable, to the outcomes achieved in the present research. In fact, Yang et al. did not pre-heat the build platform (they imposed a base plate temperature of 65 °C) and they thermally post-processed the samples. To the contrary, in the present contribution no stress relief nor thermal treatment was required, since the build platform was pre-heated to 200 °C, which served to minimize residual stresses. These two different manufacturing procedures also imply different potential applications, since aluminum-based parts in the T6 state, like those described by Yang et al., can also be addressed to high-temperature working conditions on account of the additional treatment they received. The samples presented here are instead in their as-built state and therefore their production is cheaper, but their application is limited to low-temperature conditions. Moreover Yang et al. [36] performed their fatigue tests at a frequency of 100 Hz, whereas the present parts were tested at 5 Hz. It is therefore expected that the response might be different and, from this point of view, the analysis of the effect of frequency on fatigue phenomena could be the subject for future additional investigations on A357.0 parts produced by AM techniques.



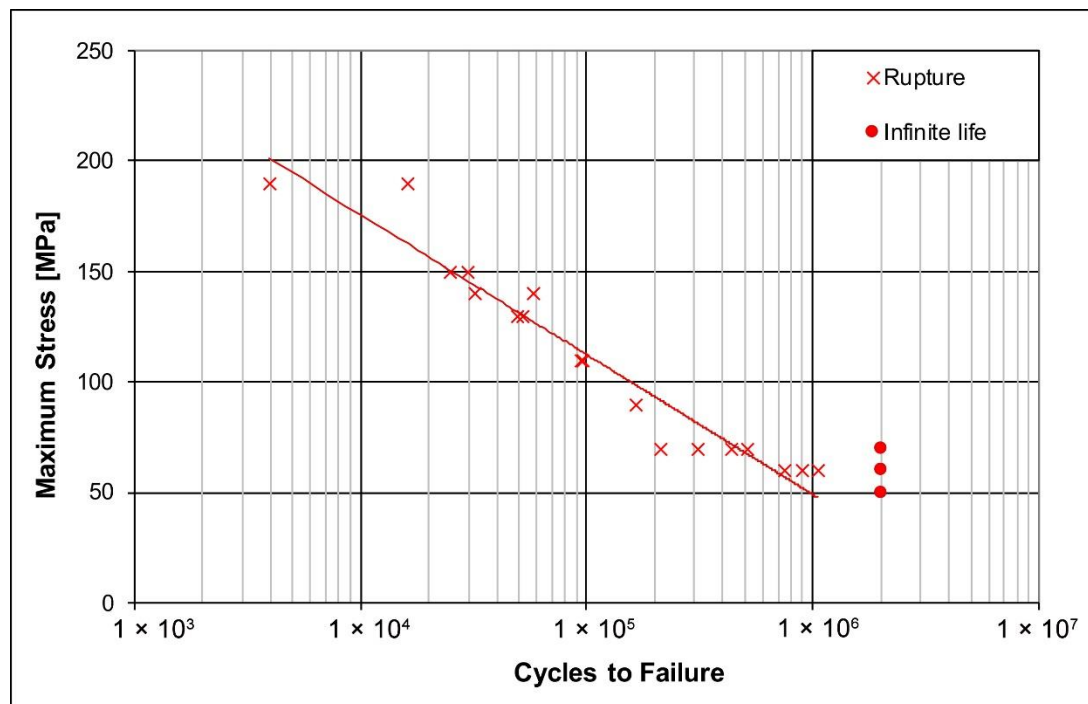
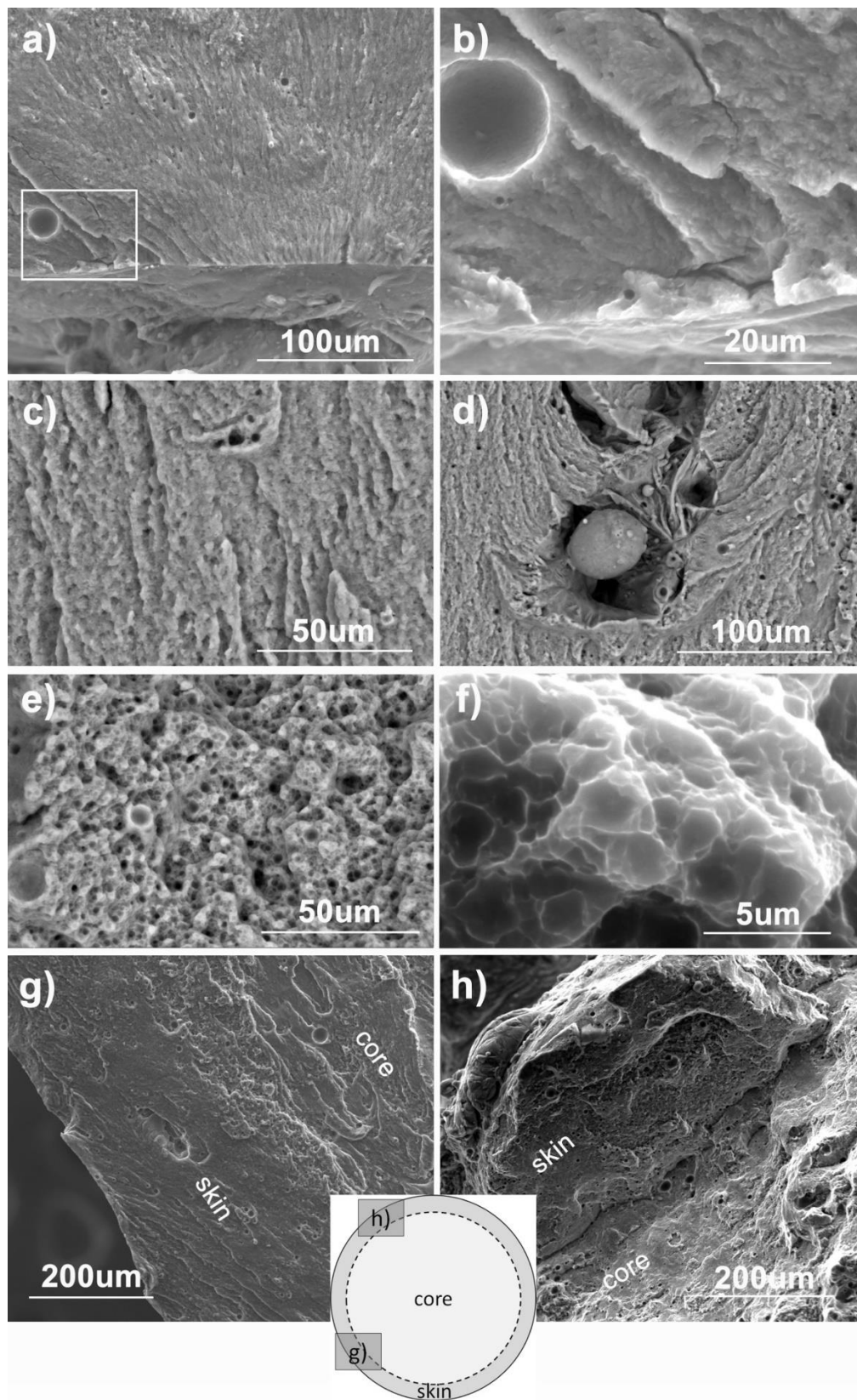


Figure 4. Wohler diagram for as-built A357.0 parts.

Regarding the analysis of the fracture surfaces, as displayed in Figure 5, the failure under high-cycle fatigue conditions starts at a sub-surface crack (Figure 5a) in proximity to an entrapped porosity (detail in Figure 5b). This confirms the role of sub-surface pores in the fatigue failure mechanism of A357.0 parts processed by L-PBF, as already observed in the past by Yang et al. [36]. The rupture morphology in the mid zone appears as in Figure 5c, with the exceptional evidence of a lack of fusion (detail in Figure 5d). In fact, in spite of the process optimization, some isolated defects caused by a lack of fusion could be observed in the finished parts. According to Yang et al., the most frequent defects in as-processed SLM parts are irregularly shaped defects, usually large in size and sometimes aligned along the building direction, which Yang et al. attributed to the lack of fusion. As stated by Yang et al. [36], such defects can be significantly reduced but not completely eliminated, even if process parameters are optimized. Generally speaking, despite process optimization, numerous and often unavoidable defects affect L-PBF aluminum parts. As a result, several authors agree that achieving defect-free AM Al parts is still beyond the current processing standards and can be anticipated in the near future [3,43,44]. As an example, minimizing porosity has been repeatedly recognized as a major challenge [11]. In any case, it is worth noting that, in the A357.0 parts investigated here, defects associated with the lack of fusion were not observed to trigger failure initiation. The latter result is particularly noteworthy if the classification of defects and their effect on mechanical response proposed by Zhang et al. is considered [44]. In fact, Zhang et al. ascribe a major role in fatigue failure to the lack of fusion defects, as compared to sub-surface round pores whose effect is less harmful. Since in the present contribution a lack of fusion is never observed as a cause of crack initiation, it can be concluded that the presence of such defects is extremely rare. The portion of the cross-section that breaks last shows a cellular fracture, typical of multi-phase materials (Figure 5e) [45]. Extremely fine hexagonal domains are observed that are known in the literature to be due to silicon precipitates at the boundaries of a cellular microstructure (Figure 5f) [45]. Apart from the failure initiation point, the rest of the rupture surface presents two different morphologies in the skin and core areas, with a distinction that becomes more and more evident at increasing distance from the failure initiation point (Figure 5g,h).



**Figure 5.** Fractography of a specimen broken under high-cycle fatigue conditions at 60 MPa: (a,b) crack initiation site; (c,d) rupture morphology in the mid zone; (e,f) cellular fracture; (g,h) morphology in the skin versus core areas.

If the specimens tested under low-cycle fatigue conditions are considered, a similar start to the failure mechanism is observed, as exemplified in Figure 6a,b. The intermediate zone is almost absent and ductile failure is observed in the greatest part of the specimen section (details provided in Figure 6c,d).

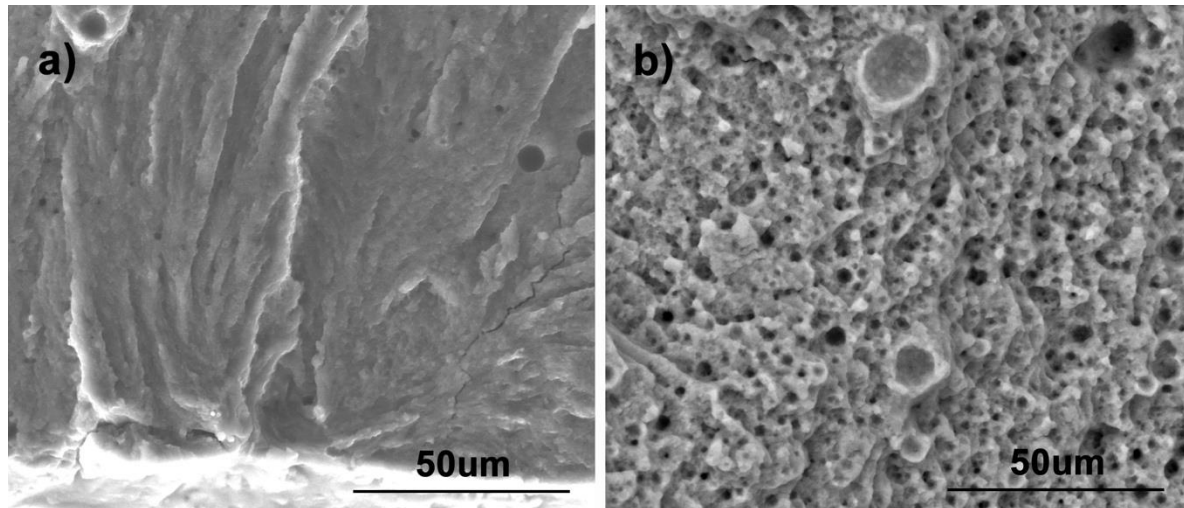


**Figure 6.** Fractography of a specimen broken under low-cycle fatigue conditions at 130 MPa: (a) crack initiation site; (b) cellular fracture.

#### 4. Conclusions

On account of the increasing need for new feedstock materials for AM and related information about their mechanical performance, the fatigue behavior of A375.0 parts produced via laser-based powder bed fusion was investigated by means of two combined approaches. The Wohler diagram was drawn according to UNI EN 3987:2010 up to  $2 \times 10^6$  cycles, which was considered as the infinite lifetime limit. The fatigue strength at  $2 \times 10^6$  cycles was instead statistically analyzed according to ISO 12107:2012, thus obtaining a mean value of 60 MPa and a standard deviation of 5.3 MPa. The samples were tested in their as-built state, thus validating their reliability as well as providing a benchmark for industrial applications and for potential future comparative analyses, including the effect of specific thermal treatments.

**Author Contributions:** Conceptualization, E.B. and A.C.; Methodology, E.B.; Validation, L.D. and E.T.; Formal Analysis, A.S.; Investigation, L.D. and E.T.; Data Curation, E.T. and L.D.; Writing—Original Draft Preparation, A.S.; Writing—Review and Editing, E.B. and A.S.; Supervision, A.C.; Project Administration, A.C.

**Funding:** This research received no external funding.

**Acknowledgments:** Andrea Pasquali, general manager of ZARE Srl (Boretto—RE, Italy), is gratefully acknowledged for the technical support and for the construction of the specimens.

**Conflicts of Interest:** The authors declare no conflict of interest.

#### References

1. Additive Manufacturing of Aluminum Alloys. Augmenting or Competing with Traditional Manufacturing? Available online: <https://www.lightmetalage.com/news/industry-news/3d-printing/article-additive-manufacturing-of-aluminum-alloys/> (accessed on 20 June 2018).
2. Brøtan, V.; Fahlströöm, J.; Sørby, K. Industrialization of metal powder bed fusion through machine shop networking. *Procedia CIRP* **2016**, *54*, 181–185. [CrossRef]
3. Iebba, M.; Astarita, A.; Mistretta, D.; Colonna, I.; Liberini, M.; Scherillo, F.; Pirozzi, C.; Borrelli, R.; Franchitti, S.; Squillace, A. Influence of powder characteristics on formation of porosity in additive manufacturing of Ti-6Al-4V components. *J. Mater. Eng. Perform.* **2017**, *26*, 4138–4147. [CrossRef]

4. Wohlers Associates. Available online: <https://wohlersassociates.com/press74.html> (accessed on 20 June 2018).
5. International Organization for Standardization. *ISO/ASTM 52900 Additive Manufacturing—General Principles—Terminology*; International Organization for Standardization: Geneva, Switzerland, 2015.
6. Bhavar, V.; Kattire, P.; Patil, V.; Khot, S.; Gujar, K.; Singh, R. A review on powder bed fusion technology of metal additive manufacturing. In Proceedings of the 4th International Conference and Exhibition on Additive Manufacturing Technologies-AM-2014, Bangalore, India, 1–2 September 2014.
7. Gibson, I.; Rosen, D.W.; Stucker, B. *Additive Manufacturing Technologies—Rapid Prototyping to Direct Digital Manufacturing*; Springer: New York, NY, USA, 2010; ISBN 978-1-4419-1119-3.
8. Tapia, G.; Elwany, A. A review on process monitoring and control in metal-based additive manufacturing. *J. Manuf. Sci. E* **2014**, *136*, 060801. [[CrossRef](#)]
9. Mower, T.M.; Long, M.J. Mechanical behavior of additive manufactured, powder-bed laser-fused materials. *Mater. Sci. Eng. A* **2016**, *651*, 198–213. [[CrossRef](#)]
10. Siddique, S.; Imran, M.; Wycisk, E.; Emmelmann, C.; Walther, F. Fatigue assessment of laser additive manufactured AlSi12 eutectic alloy in the Very High Cycle Fatigue (VHCF) range up to 1E9 cycles. *Mater. Today Proc.* **2016**, *3*, 2853–2860. [[CrossRef](#)]
11. Aboulkhair, N.T.; Everitt, N.M.; Ashcroft, I.; Tuck, C. Reducing porosity in AlSi10Mg parts processed by selective laser melting. *Addit. Manuf.* **2014**, *1–4*, 77–86. [[CrossRef](#)]
12. Irrinki, H.; Dexter, M.; Barmore, B.; Enneti, R.; Pasebani, S.; Badwe, S.; Stitzel, J.; Malhotra, R.; Atre, S. Effects of powder attributes and laser powder bed fusion (L-PBF) process conditions on the densification and mechanical properties of 17-4 PH stainless steel. *JOM* **2016**, *68*, 860–868. [[CrossRef](#)]
13. Agarwala, M.; Bourell, D.; Beaman, J.; Marcus, H.; Barlow, J. Direct selective laser sintering of metals. *Rapid Prototyp. J.* **1995**, *1*, 26–36. [[CrossRef](#)]
14. Valencia, J.J.; Queded, P.N. *ASM Handbook Volume 15: Casting*, 9th ed.; ASM International: Materials Park, OH, USA, 2008; ISBN 978-0-87170-711-6.
15. Brandl, E.; Heckenberger, U.; Holzinger, V.; Buchbinder, D. Additive manufactured AlSi10Mg samples using Selective Laser Melting (SLM): Microstructure, high cycle fatigue, and fracture behavior. *Mater. Des.* **2012**, *34*, 159–169. [[CrossRef](#)]
16. Aboulkhair, N.T.; Maskery, I.; Tuck, C.; Ashcroft, I.; Everitt, N.M. Improving the fatigue behaviour of a selectively laser melted aluminium alloy: Influence of heat treatment and surface quality. *Mater. Des.* **2016**, *104*, 174–182. [[CrossRef](#)]
17. Trevisan, F.; Calignano, F.; Lorusso, M.; Pakkanen, J.; Aversa, A.; Ambrosio, E.P.; Lombardi, M.; Fino, P.; Manfredi, D. On the selective laser melting (SLM) of the AlSi10Mg alloy: Process, microstructure, and mechanical properties. *Materials* **2017**, *10*, 76. [[CrossRef](#)] [[PubMed](#)]
18. Tang, M.; Pistorius, P.C. Oxides, porosity and fatigue performance of AlSi10Mg parts produced by selective laser melting. *Int. J. Fatigue* **2017**, *94*, 192–201. [[CrossRef](#)]
19. Uzan, N.E.; Shneck, R.; Yeheskel, O.; Frage, N. Fatigue of AlSi10Mg specimens fabricated by additive manufacturing selective laser melting (AM-SLM). *Mater. Sci. Eng. A* **2017**, *704*, 229–237. [[CrossRef](#)]
20. Romano, S.; Beretta, S.; Brandão, A.; Gumpinger, J.; Ghidini, T. HCF resistance of AlSi10Mg produced by SLM in relation to the presence of defects. *Procedia Struct. Integr.* **2017**, *7*, 101–108. [[CrossRef](#)]
21. Romano, S.; Brückner-Foit, A.; Brandão, A.; Gumpinger, J.; Ghidini, T.; Beretta, S. Fatigue properties of AlSi10Mg obtained by additive manufacturing: Defect-based modelling and prediction of fatigue strength. *Eng. Fact. Mech.* **2018**, *187*, 165–189. [[CrossRef](#)]
22. Damon, J.; Dietrich, S.; Vollert, F.; Gibmeier, J.; Schulze, V. Process dependent porosity and the influence of shot peening on porosity morphology regarding selective laser melted AlSi10Mg parts. *Addit. Manuf.* **2018**, *20*, 77–89. [[CrossRef](#)]
23. Uzan, N.E.; Ramati, S.; Shneck, R.; Frage, N.; Yeheskel, O. On the effect of shot-peening on fatigue resistance of AlSi10Mg specimens fabricated by additive manufacturing using selective laser melting (AM-SLM). *Addit. Manuf.* **2018**, *21*, 458–464. [[CrossRef](#)]
24. Bagherifard, S.; Beretta, N.; Monti, S.; Riccio, M.; Bandini, M.; Guagliano, M. On the fatigue strength enhancement of additive manufactured AlSi10Mg parts by mechanical and thermal post-processing. *Mater. Des.* **2018**, *145*, 28–41. [[CrossRef](#)]

25. Tridello, A.; Biffi, C.A.; Fiocchi, J.; Bassani, P.; Chiandussi, G.; Rossetto, M.; Tuissi, A.; Paolino, D.S. VHCF response of as-built SLM AlSi10Mg specimens with large loaded volume. *FFEMS Fatigue Fract. Eng. Mater. Struct.* **2018**, in press. [[CrossRef](#)]
26. Siddique, S.; Imran, M.; Wycisk, E.; Emmelmann, C.; Walther, F. Influence of process-induced microstructure and imperfections on mechanical properties of AlSi12 processed by selective laser melting. *J. Mater. Process. Technol.* **2015**, *221*, 205–213. [[CrossRef](#)]
27. Siddique, S.; Imran, M.; Walther, F. Very high cycle fatigue and fatigue crack propagation behavior of selective laser melted AlSi12 alloy. *Int. J. Fatigue* **2017**, *92*, 246–254. [[CrossRef](#)]
28. Siddique, S.; Awd, M.; Tenkamp, J.; Walther, F. Development of a stochastic approach for fatigue life prediction of AlSi12 alloy processed by selective laser melting. *Eng. Fail. Anal.* **2017**, *79*, 34–50. [[CrossRef](#)]
29. Herzog, D.; Seyda, V.; Wycisk, E.; Emmelmann, C. Additive manufacturing of metals. *Acta Mater.* **2016**, *117*, 371–392. [[CrossRef](#)]
30. Sercombe, T.B.; Li, X. Selective laser melting of aluminium and aluminium metal matrix composites: Review. *Mater. Technol.* **2016**, *31*, 77–85. [[CrossRef](#)]
31. Kaufman, J.G. Understanding wrought and cast aluminum alloy designations. In *Introduction to Aluminum Alloys and Tempers*; ASM International: Materials Park, OH, USA, 2000; Chapter 3; pp. 23–37. [[CrossRef](#)]
32. Aversa, A.; Lorusso, M.; Trevisan, F.; Ambrosio, E.P.; Calignano, F.; Manfredi, D.; Biamino, S.; Fino, P.; Lombardi, M.; Pavese, M. Effect of process and post-process conditions on the mechanical properties of an A357 alloy produced via laser powder bed fusion. *Metals* **2017**, *8*, 68. [[CrossRef](#)]
33. Rao, H.; Giet, S.; Yang, K.; Wu, X.; Davies, C.H.J. The influence of processing parameters on aluminium alloy A357 manufactured by Selective Laser Melting. *Mater. Des.* **2016**, *109*, 334–346. [[CrossRef](#)]
34. Rao, J.H.; Zhang, Y.; Fang, X.; Chen, Y.; Wu, X.; Davies, C.H.J. The origins for tensile properties of selective laser melted aluminium alloy A357. *Addit. Manuf.* **2017**, *17*, 113–122. [[CrossRef](#)]
35. Yang, K.V.; Rometsch, P.; Davies, C.H.J.; Huang, A.; Wu, X. Effect of heat treatment on the microstructure and anisotropy in mechanical properties of A357 alloy produced by selective laser melting. *Mater. Des.* **2018**, *154*, 275–290. [[CrossRef](#)]
36. Yang, K.V.; Rometsch, P.; Jarvis, T.; Rao, J.; Cao, S.; Davies, C.; Wu, X. Porosity formation mechanisms and fatigue response in Al-Si-Mg alloys made by selective laser melting. *Mater. Sci. Eng. A* **2018**, *712*, 166–174. [[CrossRef](#)]
37. European Committee for Standardization. *Aerospace Series—Test Methods for Metallic Materials—Constant Amplitude Force-Controlled High Cycle Fatigue Testing*; UNI EN 3987; European Committee for Standardization: Brussels, Belgium, 2010.
38. Frazier, W.E. Metal additive manufacturing: A review. *J. Mater. Eng. Perform.* **2014**, *23*, 1917–1928. [[CrossRef](#)]
39. International Organization for Standardization. *Metallic materials—Tensile testing—Part 1: Method of Test at Room Temperature*; UNI EN ISO 6892-1; International Organization for Standardization: Geneva, Switzerland, 2016.
40. International Organization for Standardization. *Metallic Materials—Fatigue Testing—Statistical Planning and Analysis of Data*; ISO 12107; International Organization for Standardization: Geneva, Switzerland, 2012.
41. Lin, S.-K.; Lee, Y.-L.; Lu, M.-W. Evaluation of the staircase and the accelerated test methods for fatigue limit distributions. *Int. J. Fatigue* **2001**, *23*, 75–83. [[CrossRef](#)]
42. Pollak, R.; Palazotto, A.; Nicholas, T. A simulation-based investigation of the staircase method for fatigue strength testing. *Mech. Mater.* **2006**, *38*, 1170–1181. [[CrossRef](#)]
43. Zhang, B.; Li, Y.; Bai, Q. Defect formation mechanisms in selective laser melting: A review. *Chin. J. Mech. Eng.* **2017**, *30*, 515–527. [[CrossRef](#)]
44. Zhang, D.; Sun, S.; Qiu, D.; Gibson, M.A.; Dargusch, M.S.; Brandt, M.; Qian, M.; Easton, M. Metal Alloys for Fusion-Based Additive Manufacturing. *Adv. Eng. Mater.* **2018**, 1700952. [[CrossRef](#)]
45. Yan, C.; Hao, L.; Hussein, A.; Young, P.; Huang, J.; Zhu, W. Microstructure and mechanical properties of aluminium alloy cellular lattice structures manufactured by direct metal laser sintering. *Mater. Sci. Eng. A* **2015**, *628*, 238–246. [[CrossRef](#)]

